Nanoelectronics and Its New Materials – A NEW ERA OF NANOSCIENCE

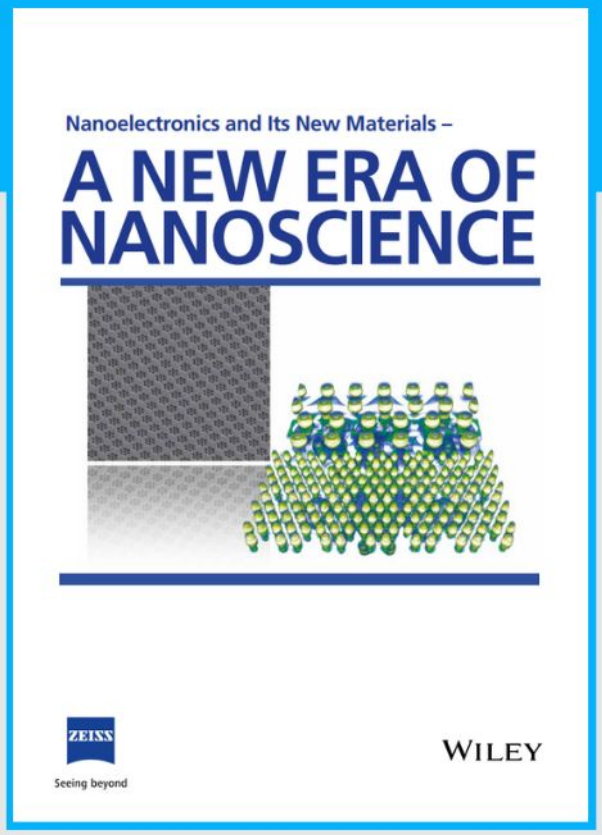

Discover the recent advances in electronics research and fundamental nanoscience.

Nanotechnology has become the driving force behind breakthroughs in engineering, materials science, physics, chemistry, and biological sciences. In this compendium, we delve into a wide range of novel applications that highlight recent advances in electronics research and fundamental nanoscience. From surface analysis and defect detection to tailored optical functionality and transparent nanowire electrodes, this eBook covers key topics that will revolutionize the future of electronics.

To get your hands on this valuable resource and unleash the power of nanotechnology, simply download the eBook now. Stay ahead of the curve and embrace the future of electronics with nanoscience as your guide.

ZEISS

Seeing beyond

WILEY

ADVANCED FUNCTIONAL MATERIALS
www.afm-journal.de

Light Controlled Biohybrid Microbots

*Nicola Pellicciotta, Ojus Satish Bagal, Viridiana Carmona Sosa, Giacomo Frangipane, Gaszton Vizsnyiczai, and Roberto Di Leonardo**

Biohybrid microbots integrate biological actuators and sensors into synthetic chassis with the aim of providing the building blocks of next-generation microrobotics. One of the main challenges is the development of self-assembled systems with consistent behavior and such that they can be controlled independently to perform complex tasks. Herein, it is shown that, using light-driven bacteria as propellers, 3D printed microbots can be steered by unbalancing light intensity over different microbot parts. An optimal feedback loop is designed in which a central computer projects onto each microbot a tailor-made light pattern, calculated from its position and orientation. In this way, multiple microbots can be independently guided through a series of spatially distributed checkpoints. By exploiting a natural light-driven proton pump, these bio-hybrid microbots are able to extract mechanical energy from light with such high efficiency that, in principle, hundreds of these systems can be controlled simultaneously with a total optical power of just a few milliwatts.

1. Introduction

Robots and artificial intelligence have now reached a level of performance where they can easily replace human workers in a wide range of jobs. As biomedical technologies provide new and reliable tools for diagnostics and therapy at the single-cell level,[1,2] micro-robots could bring automation even within miniaturised laboratories built on the slide of a microscope (lab-on-chip) or inside the human body. While modern two-photon photopolymerisation (TPP) techniques allow us to create complex 3D architectures,[3] the miniaturisation of sensors and actuators still faces difficult challenges. The bio-hybrid approach seeks to solve these challenges by exploiting the enormous wealth of biological components that cells use to probe the environment and move within it in an informed manner.[4–6] When it comes to transporting a cargo over long distances, microswimmers such as microalgae or bacteria can be attached to synthetic objects and provide propulsion speeds of up to several tens of micrometers per second.[7–10] By designing asymmetrically shaped objects, it is possible to avoid permanent attachment and simply rely on the spontaneous rectification of bacterial trajectories. This approach has been used to generate rotary[11] and linear[12–14] motions but, although easier to implement, it has significant limitations due to the enormous variability and fluctuations in propulsion characteristics. One possibility to mitigate these fluctuations is to use more controlled patterning methods to permanently attach bacteria.[15] An even more deterministic self-assembly can be achieved by exploiting the ability of TPP to fabricate 3D structures in which individual bacteria can self-locate within micro-chambers arranged in geometric arrays.[16,17] Once assembled, and in motion, the next challenge is to control the trajectories of these biohybrid micromachines. One possibility is to exploit the natural taxis mechanisms of the propelling cells to guide the entire structure through external fields such as concentration gradients (chemotaxis)[18] or magnetic fields (magnetotaxis).[19,20] External magnetic fields can also steer the microbots by acting directly on a magnetic cargo.[21] If one day, however, these microbots are to be able to be independently programmed to automatically perform a sequence of complex tasks, we will need a guidance mechanism that can operate independently on several microbots and with a sufficiently consistent response to simplify the design of a common centralized control strategy. This requires independently addressable actuators with sufficiently low energy requirements to sustain, in principle, the prolonged operation of a swarm of hundreds or even thousands of microbots.[22] These requirements can be met by *E. coli* bacteria expressing the light-driven proton pump proteorhodopsin. Each one of these cells is capable of generating a piconewton thrust force by rotating a helical flagellar bundle. Flagella are powered by electric nanomotors, the flagellar motors, which generate a torque proportional to the proton motive force (pmf) across the cell's inner membrane. In cells expressing proteorhodopsin,

N. Pellicciotta, O. S. Bagal, V. C. Sosa, G. Frangipane, G. Vizsnyiczai, R. D. Leonardo
Dipartimento di Fisica
Sapienza Universitá di Roma
Piazzale A. Moro 5, Roma 00185, Italy
E-mail: roberto.dileonardo@uniroma1.it
N. Pellicciotta, G. Frangipane, R. D. Leonardo
NANOTEC-CNR
Soft and Living Matter Laboratory
Piazzale A. Moro 5, Roma 00185, Italy
G. Vizsnyiczai
Biological Research Centre
Institute of Biophysics
Eötvös Loránd Research Network (ELKH)
Temesvári krt. 62, Szeged 6726, Hungary
The ORCID identification number(s) for the author(s) of this article can be found under https://doi.org/10.1002/adfm.202214801.

© 2023 The Authors. Advanced Functional Materials published by Wiley-VCH GmbH. This is an open access article under the terms of the Creative Commons Attribution License, which permits use, distribution and reproduction in any medium, provided the original work is properly cited.

DOI: 10.1002/adfm.202214801

when oxygen concentration is low and respiration is inhibited, the proton motive force can be regulated from zero to saturation using only a few tens of nanowatts of optical power. For comparison, if optical tweezers were used for actuation, more than 10 000 times more power would be required to generate an equivalent thrust.[23] This means that with a few milliwatts, we can control hundreds of thousands of micro-propellers. The big challenge is how to integrate these biological propellers into a microfabricated chassis to obtain programmable micro-robots.

Here, we demonstrate a prototype of a micro-vehicle powered by bacteria that can be programmed to follow a prescribed path while moving on a glass substrate in a liquid sample. These microbots consist of a microfabricated chassis with two spatially separated propulsion units, each equipped with eight bacterial slots into which smooth swimming cells can enter and remain trapped indefinitely. Using light-driven bacteria, these microbots can be individually powered by illuminating them with a spotlight, the intensity of which allows their speed to be controlled remotely. Since the two propulsion units are rigidly connected, unbalancing the light on each of them makes it possible to generate a controllable torque and steer left or right. We deploy these microbots using a centralised control strategy in which a computer vision system tracks multiple units and calculates an optimised light pattern to guide them independently along a predefined path. Finally, we discuss how to optimise the control strategy in terms of target pointing stability and target orbiting.

2. Results and Discussion

2.1. Microbot Structure

We designed self-propelled microbots that can be independently steered along 2D trajectories on a solid substrate, typically the bottom glass of a microfluidic chip. **Figure 1**a shows a schematics of the microbot structure. The microbot is composed of two identical units, named here propellers or engines, connected by a 20 µm-long rod. Each unit has the shape of a rectangular box 18.6x5.0x6.1 µm^3 (LxWxH) and is composed of eight microchambers. The microchambers have openings of 2.8x3.5 µm (WxH) to accommodate a single cell body while leaving the entire flagellar bundle outside for maximal propulsion. The chambers are arranged symmetrically to the major axis of the engine and tilted by 45° to maximize the total force applied on the engine.[17]

We used two-photon polymerization to fabricate the microbots chassis from SU-8 photoresist.[3] A SEM image of a fabricated structure is shown in (Figure 1b) together with the actual main geometrical dimensions. Arrays of structures are fabricated on top of coverglasses that were previously coated with a sacrificial layer of dextran.[24]

As light controlled propellers, we use a smooth swimming strain of *E. coli* bacteria expressing the light-driven proton pump proteorhodopsin.[25] In the absence of oxygen, aerobic respiration is blocked and proteorhodopsin can be used to control the proton motive force that drives the flagellar motors, so that the cell's speed becomes a function of the local intensity of green light.[25] When the aqueous solution containing the bacteria is introduced into the chamber, the dextran layer dissolves and the structures detach from the cover glass. Based on the measurements in Figure 1b, we estimate a total volume of 10^3 µm^3 resulting in a buoyant mass of 0.2 ng (SU-8 density 1.2 g cm^{-3}) and therefore a small sedimentation length $k_BT/mg = 2$ nm that keeps the empty chassis fully sedimented on the bottom coverglass. The self-assembly of the bacteria in the microchambers is remarkably efficient and is completed within minutes. Similar efficiency had previously been reported for even more complex three-dimensional structures.[17] In this case, self-assembly is further facilitated by the fact that the structures sit on the plane of the cover glass, where the concentration of bacteria is highest due to hydrodynamic entrapment.[26] Furthermore, we

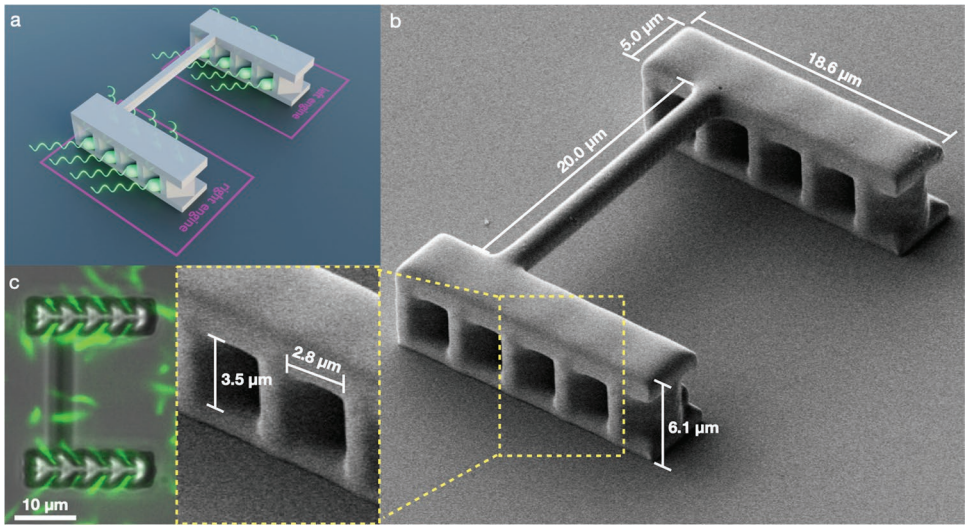

Figure 1. 3D microbot chassis a) Schematic representation of a self assembled bio-hybrid microbot with *E. coli* bacteria appearing in green. b) SEM image of the 3D chassis with a zoomed view of the yellow box. c) Fluorescent bacteria (green channel) are superimposed on a bright-field image of the chassis to show that all microchambers are occupied. Bacteria swimming outside of the microchambers are not permanently embedded in the chassis, but are free to swim away after brief interactions.

© 2023 The Authors. Advanced Functional Materials published by Wiley-VCH GmbH

16163028, 0, Downloaded from https://onlinelibrary.wiley.com/doi/10.1002/adfm.202214801 by University Di Roma La Sapienza, Wiley Online Library on [11/09/2023]. See the Terms and Conditions (https://onlinelibrary.wiley.com/terms-and-conditions) on Wiley Online Library for rules of use; OA articles are governed by the applicable Creative Commons License

believe that the bacteria's tendency to swim with a direction of propulsion inclined toward the interior of the confining walls, might play an important role in getting into the micro-chambers when cell slide along the side walls.[26,27] When loaded with bacteria the microbots self-propel with an average speed of 2 μm s^{-1} tracing circular paths that remain confined on the glass surface. As for freely swimming bacteria, these microbots will be force free and thus generate dipolar fluid flows that when reflected by the no-slip boundary at their bottom, will give rise to a hydrodynamic attraction stabilizing the confinement of the microbot in the 2D plane.[28]

2.2. Microbot Dynamics

Our microbots can only translate on the 2D plane defined by the coverslip surface and rotate around the normal to that surface. Calling $\Gamma_{\parallel}$ the translational drag of a single structure moving along its axis, Γ_z its rotational drag around a vertical axis passing through the center and $2L = 25\,\mu m$ the distance between the two engine axes, we can write the microbots linear speed v and angular speed ω as:

$$v = \frac{1}{\Gamma_{\parallel}}(f_R + f_L) \tag{1}$$

$$\omega = \frac{L}{\Gamma_z}(f_R - f_L) + \frac{1}{\Gamma_z}(\tau_R + \tau_L) \tag{2}$$

with f_R, f_L being the total forces and τ_R, τ_L as the torques applied by bacteria on the right and left engines respectively. In a perfectly symmetrical system, under homogeneous green light illumination, one would expect the bacteria to apply zero torque and equal forces on the two units, thus propelling the microbot on a straight path. In reality, we always observe circular trajectories as shown in **Figure 2**a and Video S1 (Supporting Information). As expressed in Equation 2, this non-zero angular velocity may be due to an asymmetry between f_R and f_L or to net torques τ_R, τ_L applied by the bacteria on the individual engines. These torques may result from an asymmetric distribution of forces on each motor due to the natural variability of the thrust force generated by individual bacteria. In addition, since to facilitate loading, the size of a microchamber is designed to loosely accommodate a single cell, we cannot exclude that more than one cell may occasionally fit into a slot. Net torques on the propellers may also arise from the inevitable roto-translational coupling with the substrate, which is also responsible for the clockwise motion of bacteria over solid walls.[29]

However, we observe circular trajectories running both clockwise and counterclockwise with no clear systematic effect suggesting that roto-translational couplings do not play a major role here. The trajectories of these uncontrolled microbots also show the presence of noise, which we quantified by calculating the variance of angular displacement as a function of time. (Figure 2b). A clear linear increase can be seen, indicating the presence of a diffusive term in the angular displacement, superimposed on the average rotation.

The force generated by each engine has the same dependence on light intensity as individual cells[25,30,31] which can be modeled by:

$$f(I) = f_0 \frac{I}{I + K} \tag{3}$$

Where I is the power density of the projected green light and K a threshold value such that when $I \gg K$ proteorhodopsins photocurrents are saturated, and bacteria trapped inside microchambers transfer a total maximal thrust f_0 on each engine. For the following discussion, we will only consider symmetric microbots so that we can neglect τ_R and τ_L and

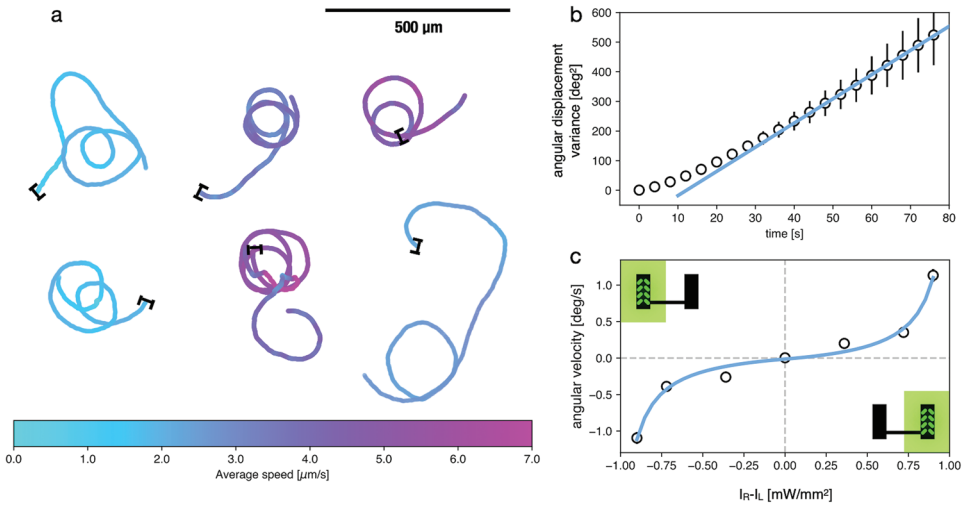

Figure 2. Uncontrolled microbot dynamics a) When exposed to a uniform illumination, microbots tend to follow circular trajectories due to the natural propulsion variability of bacteria filling the two engines. Line colors encode instantaneous speed as indicated in the colorbar. b) The variance of angular displacement as a function of elapsed time evidences the presence of fluctuating noise as a diffusive term that increases linearly with time. Circles represent an average over time origin and over seven microbots. Error bars are the standard error of the mean. c) Angular speed as a function of the difference in light intensity between the right and left engine. Solid line is the least-squared fit with the model expressed in Equation 5 and discussed in the text.

© 2023 The Authors. Advanced Functional Materials published by Wiley-VCH GmbH

16163028, 0, Downloaded from https://onlinelibrary.wiley.com/doi/10.1002/adfm.202214801 by University Di Roma La Sapienza, Wiley Online Library on [11/09/2023]. See the Terms and Conditions (https://onlinelibrary.wiley.com/terms-and-conditions) on Wiley Online Library for rules of use; OA articles are governed by the applicable Creative Commons License

assume $f_R = f(I_R)$, $f_L = f(I_L)$. Substituting into the expressions for the linear (Equation 1) and angular (Equation 2) speeds of the microbot, we obtain:

$$v = \frac{v_0}{2}\left(\frac{I_R}{I_R+K}+\frac{I_L}{I_L+K}\right) \tag{4}$$

$$\omega = \omega_0\left(\frac{I_R}{I_R+K}-\frac{I_L}{I_L+K}\right) \tag{5}$$

where we introduced the maximum values for the linear speed $v_0 = 2f_0/\Gamma_{\parallel}$ and angular speed $\omega_0 = f_0 L/\Gamma_z$. The former is achieved when the light intensities on both engines are much greater than the threshold value K for proteorhodopsin saturation, while maximum angular speed is reached when the light intensity is well above the threshold on one engine and zero on the other one. We measured the angular velocity of the microbots in the presence of an unbalanced illumination on the two engines. Averaging over time and over several microbots, we obtained the data shown as circles in Figure 2c. The expression in Equation 5 provides an excellent fit for experimental data (blue line in Figure 2c), with best fit parameters $\omega_0 = 1.30 \pm 0.07$ deg s^{-1} and $K = 0.17 \pm 0.05$ mW mm^{-2}. The latter K parameter is consistent with previous studies on light-driven propulsion in *E. coli*.[25,31]

2.3. Navigation Strategy

At this point, we want to find an optimal strategy to control the power of the two engines in order to drive a microbot toward a predefined target. Indicating with $\mathbf{r}$ the microbot position vector measured from the target and with $\hat{\mathbf{e}}$ its orientation, **Figure 3**a, we can define the angular distance from the target as the angle θ between directions $-\hat{\mathbf{r}}$ and $\hat{\mathbf{e}}$. Following,[32] the time evolution of θ will be given by:

$$\dot{\theta} = \omega(\theta) + \frac{v(\theta)\sin\theta}{r} \tag{6}$$

The functions $\omega(\theta)$ and $v(\theta)$ represent the angular and linear speeds of the microbot. From Equation 2, these are set externally by choosing the appropriate response functions $f_R(\theta)$ and $f_L(\theta)$ to be imposed on the two engines according to the measured value of the angular distance from the target θ. Under uniform saturating illumination, a symmetric microbot will have $f_R = f_L = f_0$ resulting in a constant linear speed $v_0 \propto f_R + f_L$ and a vanishing angular speed $\propto f_R - f_L$. Unless the microbot was initially pointing toward the target ($\theta = 0$) the angular distance will eventually approach the stable value $\theta = \pi$ with the microbot moving far away from the target. If we want to automatically reach the target we need to find a proper navigation strategy encoded in the functions $f_R(\theta), f_L(\theta)$. The first condition to be

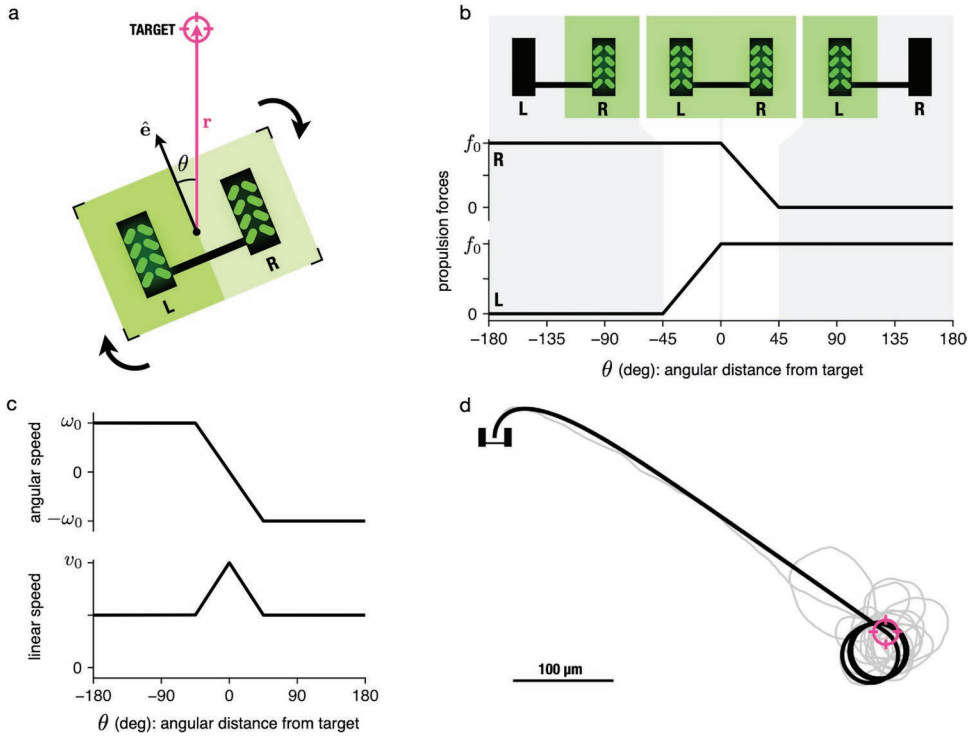

Figure 3. Navigation strategy. a) Definition of geometric variables. b) Dependence of left and right force on angular distance from target. When the microbots point in a direction more than 45 degrees away from the target, one motor is switched off while the other runs at maximum speed, achieving maximum torque. For deviations of less than 45 degrees one of the two engines is progressively turned off with a linear dependence on θ. c) Angular and linear speed as a function of angular distance θ when right and left forces are set as in b). d) A numerical calculated trajectory using ω_0 and v_0 parameters as extracted from experiments. The microbot points to the target and then settles in a circular eccentric orbit around it. Gray line is a simulation with the same parameters plus rotational diffusion with diffusivity extracted from the fit in Figure 2b.

© 2023 The Authors. Advanced Functional Materials published by Wiley-VCH GmbH

16163028, 0, Downloaded from https://onlinelibrary.wiley.com/doi/10.1002/adfm.202214801 by University Di Roma La Sapienza, Wiley Online Library on [11/09/2023]. See the Terms and Conditions (https://onlinelibrary.wiley.com/terms-and-conditions) on Wiley Online Library for rules of use; OA articles are governed by the applicable Creative Commons License

16163028, 0, Downloaded from https://onlinelibrary.wiley.com/doi/10.1002/adfm.202214801 by University Di Roma La Sapienza, Wiley Online Library on [11/09/2023]. See the Terms and Conditions (https://onlinelibrary.wiley.com/terms-and-conditions) on Wiley Online Library for rules of use; OA articles are governed by the applicable Creative Commons License

met is that the aiming toward the target is stable or equivalently that $\theta = 0$ is a stable fixed point of Equation 6. For small θ we can expand $\omega(\theta) \approx -\omega_0'\theta$ and $v(\theta) \approx v_0$ to linearize Equation 6:

$$\dot{\theta} = -\left(\omega_0' - \frac{v_0}{r}\right)\theta \tag{7}$$

As already discussed in [32], stability requires that $\omega(\theta)$ has a steep negative slope so that $\omega_0' > v_0/r$. The angular speed can only be modulated in a finite range of values $[-\omega_0, \omega_0]$ whose extremes are reached when one motor is running at full power f_0 and the other one is off resulting in $\omega_0 = f_0 L/\Gamma_z$ (Equation 2). To ensure aiming stability, it is therefore advisable to increase the slope of $\omega(\theta)$ around $\theta = 0$ by concentrating the entire dynamic range in a restricted angular interval $[-\theta_0, \theta_0]$. This can be achieved by choosing the functions $f_R(\theta)$ and $f_L(\theta)$ as in Figure 3b. The angular speed will then have a constant slope $\omega_0' = \omega_0/\theta_0$ throughout the interval $[-\theta_0, \theta_0]$, see Figure 3c.

With this choice for $f_R(\theta)$ and $f_L(\theta)$, aiming stability, as established by Equation 6, will be guaranteed until the distance to the target falls below a critical value:

$$r_c = \frac{v_0}{\omega_0'} = \frac{2\Gamma_z}{L\Gamma_{\parallel}}\theta_0 \tag{8}$$

If we aim for a minimum approach distance to the target of less than r_c, the microbot may miss the target and move away from it indefinitely before returning back.[32] However, if we use $f_R(\theta)$ and $f_L(\theta)$ as in Figure 3b, that is, such that the angular velocity is maximum when $|\theta| > \theta_0$ (Figure 3c), then the microbot will hold in an eccentric circular orbit around the target with a minimum approach distance given by $r_c \cos\theta_0/2\theta_0$. In our case, we choose $\theta_0 = \pi/4$, so the minimum approach distance is $\simeq r_c/2$.

Real systems will always be affected by a substantial amount of noise from thermal agitation and fluctuations in the propelling force and arrangement of bacteria. In a noisy environment, pointing stability is an even more crucial requirement, and failure to reach the target due to random reorientation requires efficient mitigation strategies to keep the orbit confined within a narrow target zone (Figure 3d).

2.4. Automated Optical Control of Multiple Microbots

We couple a DLP (Digital Light Processing) projector to the microscope objective to address individual microbots with independently controlled illumination on the two engines. Using the same objective for imaging and projection allows us to shape the speed of bacteria with a spatial resolution that matches that of the imaging system.[31,33] Multiple microbots can be controlled simultaneously by a central computer that continuously monitors their positions and calculates tailor-made light patterns to guide them along a pre-programmed task. In this work, we concentrate on path planning; that is, moving microbots through a sequence of target destinations. To this end, a computer vision algorithm tracks the position and orientation of microbots and computes the angular distance θ from the next target. We then calculate the intensities on the right and left engines in order to implement the navigation strategy $f_R(\theta)$, $f_L(\theta)$ illustrated in Figure 3b. When $|\theta| > \theta_0 = 45°$, one engine is turned off while the other one runs at full power so that the microbot rotates at maximum speed to decrease the angular distance to the target. When $|\theta| < \theta_0$, we always keep one engine at full power while lowering light intensity on the other one with a linear dependence on θ (see Figure 3b). As discussed before, this choice of navigation strategy guarantees aiming stability and also confined orbiting around the target. We defined a path consisting of three non-aligned targets A,B,C placed at a relative distance of approximately 500 µm (**Figure 4**a). When the distance to the target falls below 50 µm, the microbot turns to reach the next target along the path. Eventually, the final target C is reached, light is turned off on both engines and the microbot stops. Figure 4a shows a sample trajectory of a microbot. The black arrows represent the orientation of the microbot, while the magenta arrows point to the target. For most of the trajectory, the black arrow is rotated counterclockwise relative to the direction of the target (positive angular distance θ) and must be corrected with a negative rotation (clockwise). This is most clearly depicted in Figure 4b showing the time evolution of the angular velocity of the same microbot. The latter closely resembles the modulation of the difference between the light intensities projected on the left and right engines also reported in figure. Figure 4c shows the trajectories of seven microbots navigating through the same three-target path. The colours of the lines encode the average speed over the entire path. Depending on their initial position and orientation, the seven microbots reach the first target (A) following very different paths. When they move toward B, they all start from neighboring positions, so that their trajectories wander a little less. In the last stage, since they all arrived at B from A, they also share more similar initial orientations, so that the final paths seem less dispersed and more straight. The completion time for this task ranges from 10 to 20 min depending on the microbot, with an average value of 13 min. In general, the faster microbots appear to wander more and reach the final target after travelling a greater total distance. In Figure 4d, we report the contour length of each trajectory, normalised to the minimum distance given by the length of the straight paths joining the target centers (black line). Because target regions are not point-like, some trajectories may be shorter than the distance between target centers. Interestingly the dispersion of the total travelled distance is only of about a few 10%. Moreover, almost all of the shuttles travelled a total distance greater than the optimum by only 2%-15%. This distance is clearly correlated to microbot speed with the slower shuttles staying closer to the optimal trajectory. This observation may seem to be in agreement with what was already pointed out in [32] and expressed by Equation 7, namely that a higher velocity v_0 reduces the stability of pointing. It should be noted, however, that in our case, v_0 and ω_0 should vary in a correlated way being both proportional to f_0. One possible explanation for the increased tortuosity of fast microbots could be that the propulsion of each motor fluctuates with multiplicative noise.

The main advantage of using light as an external control field is that multiple microbots can be controlled independently to collaborate on the same task. To demonstrate this, we simultaneously programmed two microbots to move along the same three targets path. **Figure 5** shows four frames of Video S2 (Supporting Information) showing two

© 2023 The Authors. Advanced Functional Materials published by Wiley-VCH GmbH

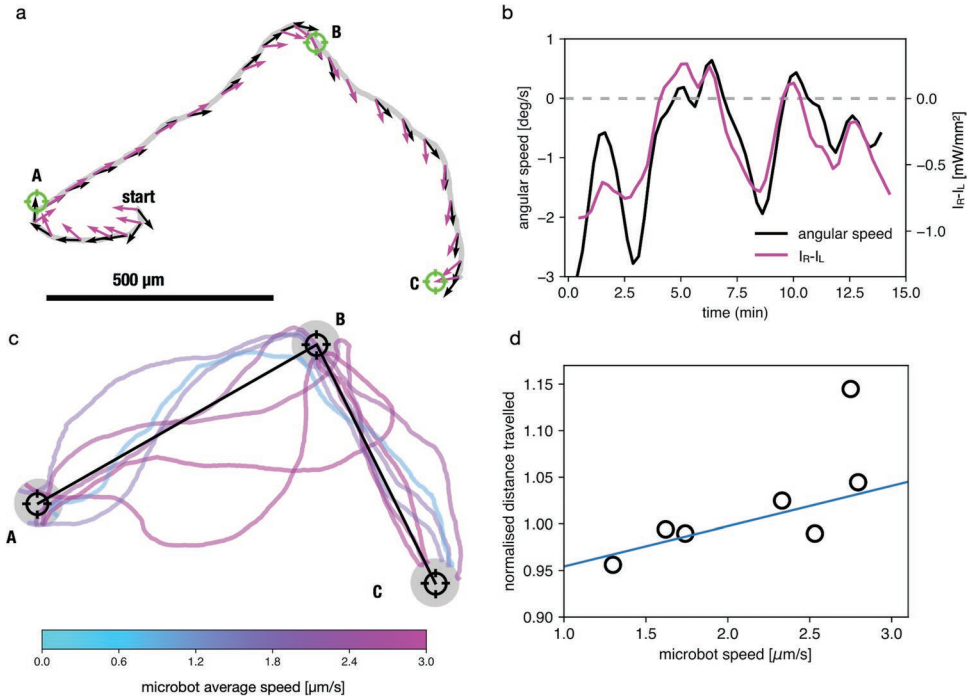

Figure 4. Path planning a) Sample trajectory of a microbot following a path consisting of three non-aligned targets A,B,C. Black arrows indicate microbot orientation $\hat{\mathbf{e}}$ while magenta arrows point to the target. b) The angular speed along the microbot trajectory shown in (a) is reported in black together with the right/left imbalance of light intensity on the two engines (magenta). c) Different microbots performing the same three target task (n=7). Line colors encode mean speed as indicated in the colorbar. d) Total traveled distance shows a weak correlation with microbot average speed.

microbots independently programmed to move from one target to another. Again, as with the individually guided microbots in Figure 4c, we note that while from A to B the trajectories are quite far apart, in the last section they become very close. The central control algorithm ignores possible collisions between two microbots. These aspects could become important when the number of microbots grows, but fortunately, their management would only require a modification of the algorithm by introducing, for example, effective interactions that mimic visual perception between the different microbots.[34]

2.5. Efficiency and Optimization

Using simple scaling arguments, we can discuss the possibility of scaling up the size of our microbots. For example, by increasing the length of the engine we could accommodate more microchambers, the number of bacteria would increase, and proportionally so would the applied thrust f_0. At the same time, the translational viscous drag $\Gamma_{\parallel}$ would also increase linearly with the propeller length so that the propulsion speed would not change with size. Thus, there is no clear advantage in increasing the size of the propulsion units, especially considering that one of the most promising applications for the microbots might be in single-cell transport. For a fixed propeller size the distance between the two units should be chosen in order to increase the steering speed Ω. Calling $\gamma_{\parallel}$ and γ_z the translational and rotational drag of the isolated left and right units, we can obtain the drag on the composed structure as a function of the distance L:[35]

$$\Gamma_{\parallel} = 2\gamma_{\parallel}, \Gamma_z = 2(\gamma_z + L^2\gamma_{\parallel}) \tag{9}$$

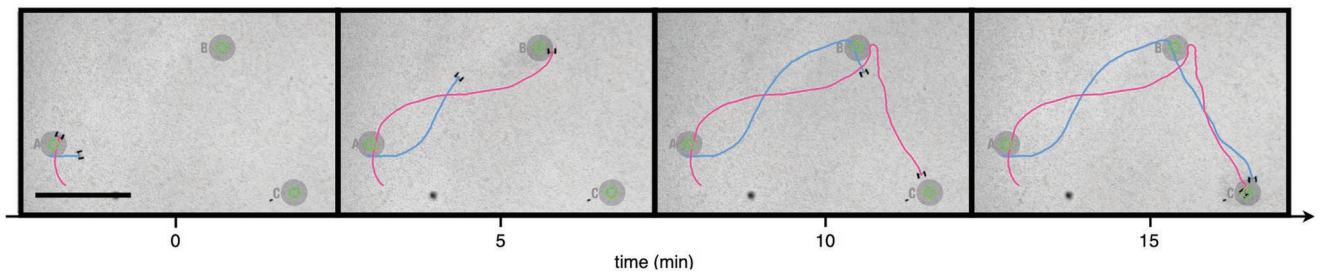

Figure 5. Simultaneous control of multiple microbots. Frames from Video S2 (Supporting Information) showing two microbots that are being simultaneously programmed to perform the three-target task. Scale bar on the first frame is 200 µm.

© 2023 The Authors. Advanced Functional Materials published by Wiley-VCH GmbH

16163028, 0, Downloaded from https://onlinelibrary.wiley.com/doi/10.1002/adfm.202214801 by University Di Roma La Sapienza, Wiley Online Library on [11/09/2023]. See the Terms and Conditions (https://onlinelibrary.wiley.com/terms-and-conditions) on Wiley Online Library for rules of use; OA articles are governed by the applicable Creative Commons License

16163028, 0, Downloaded from https://onlinelibrary.wiley.com/doi/10.1002/adfm.202214801 by University Di Roma La Sapienza, Wiley Online Library on [11/09/2023]. See the Terms and Conditions (https://onlinelibrary.wiley.com/terms-and-conditions) on Wiley Online Library for rules of use; OA articles are governed by the applicable Creative Commons License

where we have neglected hydrodynamic interactions between the two units (see Section S1.1, Supporting Information). We can then express the maximum angular speed ω_0 as a function of L

$$\omega_0 = \frac{f_0 L}{\Gamma_z} = \frac{f_0 L}{2(\gamma_z + L^2\gamma_\parallel)} \tag{10}$$

where $f_0 L$ is the maximum torque applied by the bacteria. We find that there's an optimal value for L which maximizes ω_0 and it is given by $\sqrt{\gamma_z/\gamma_\parallel}$. Experimental estimates for $\gamma_\parallel$ and γ_z confirm that our choice for L is very close to this optimal value (see Section S1.1, Supporting Information). Let us now turn to energy considerations. Within our microbots, bacteria work to push the SU-8 chassis at a speed $v \simeq 2$ μm/s. The viscous medium resists this motion with a drag coefficient $\Gamma_\parallel = 0.67$ pN sμm^{-1} that we extracted from the Brownian mean square displacement of the empty structures (see Section S1.2, Supporting Information). The energy output can be defined as the mechanical work performed by the bacterial thrust $P_{out} = \Gamma_\parallel v^2 \simeq 3$ aW. On the input side, flagellar motors are ultimately powered by projected light whose integrated flux over the two engines running at maximum power is about $P_{in} = 100$ nW resulting in an overall efficiency of light to work conversion of $3 \cdot 10^{-11}$. This figure is consistent with that reported for rotary machines actuated by light-driven bacteria[17] and, as already discussed there, it is orders of magnitude larger than the efficiency of light-driven micromachines actuated by radiation pressure.[36,37]

3. Conclusion

We show how photokinetic bacteria can self-organize within a 3D microfabricated structure to produce a light-controlled microbot. These microbots can be individually programmed by a central computer to move over a sequence of checkpoints located arbitrarily over a millimeter-sized area on a microscope cover glass. In addition to acting as a remote control of the microbots' direction, the light also provides the energy needed to generate self-propulsion. Previously proposed light-controlled biohybrid microbots used light as an on/off switch to control unidirectional rotational or translational motion.[38,39] Other possible strategies for using light to guide microbots on a prescribed path involve the use of focused laser light to generate propulsion through cavitation-induced flows[40] or radiation pressure.[41] Typical power in these cases is on the order of tens of milliwatts per microstructure, whereas our microbots can operate with less than a microwatt of total power. This is due to the high efficiency of proteorhodopsin in converting energy from optical to electrochemical, so in principle it is possible to control hundreds of these microbots using only a few milliwatts of light, thus avoiding photodamage in biological applications and paving the way for swarm micro-robotics in lab-on-chip.

4. Experimental Section

Materials: SU-8 2015 and its standard SU-8 developer solution were purchased from KAYAKU Advanced Materials. Dextran (a polymer of anhyroglucose ($C_6H_{10}O_5$)) from *Leuconostoc mesenteroides* was procured from Sigma-Aldrich. The dextran solution was prepared in the following way: 250 mg of dextran was dissolved in 10ml of deionized water and placed in a water bath at 95°C for 30 min. The resulting solution, having a final concentration of 2.5% w/v, was passed through a sterile filter with pore sizes of 0.45 μm before use. Glass coverslips used for microfabrication were cleaned with piranha wet etch solution. This is prepared by dissolving NoChromix reagent (Godax laboratories) in Sulphuric acid (H_2SO_4, 95.0-98.0%, Sigma–Aldrich) in a 5% w/v concentration. Bacteria were grown in Terrific Broth (TB), an enriched growth medium. For TB preparation, we dissolve 2.4 grams of tryptone (Sigma–Aldrich), 4.8 grams of yeast extract (Sigma-Aldrich), and 919 μl of glycerol ($C_3H_8O_3$, 87%, Sigma–Aldrich) in 200 ml of deionized water (H_2O). The solution is stirred until it becomes homogeneous and is autoclaved for sterilization at 125°C for 15 min. All chemicals were used as received without any further purification.

SU-8 Layers Preparation: The fabrication of microbots was done on soda lime glass substrates of thickness 0.13–0.17 μm. The removal of surface impurities was done by placing the glass substrate in a piranha wet etch solution for a period of 24 h. After this, the substrate undergoes multiple rinse cycles in deionized water and was dried before plasma treatment for 10 min to increase the surface's wettability and allow the polymers to spread uniformly.[42] First, 300 μl of Dextran solution (2.5% w/v) was spin-coated on the substrate at 1000 rpm for 15 s and heated for 2 min at 95°C. This layer provides a water-soluble sacrificial layer to lift off the microbot easily.[24] On top of this Dextran layer, the 300 μl SU-8 photoresist was spin coated using two different speeds; first at 500 rpm for 10 s and later at 2000 rpm for 30 s. After the deposition of the SU-8 layer, the substrate undergoes soft-baking at 95°C for 30 min to evaporate the excess solvent. The resulting SU-8 layer measures approximately 25 μm in thickness. A schematic of the sample was illustrated in Figure S2 (Supporting Information).

Two Photon Polymerization Setup: The microbots were fabricated on a custom-built two-photon polymerization setup (TPP).[17] The laser has a wavelength of 780 nm with 87 fs pulse duration, 80 Mhz repetition rate, and 160 mW optical power (FemtoFiber pro NIR, TOPTICA Photonics AG). The objective used during the microfabrication process was a Nikon 60x oil immersion (1.4 N.A.). An optical shutter regulates the exposure time of the laser. The translation of the laser spot was controlled by a piezo stage (P563.3CD, Physik Instrumente (PI) GmbH & Co. KG) that has a three-axis translation of up to 300 μm. The piezo and optical shutter were controlled remotely through a NI-DAQ DA card.[17]

Microbot Fabrication: The SU-8 layers were used for the microfabrication process in the TPP. The scanning speed and power of the laser were maintained at 40 μm s^{-1} and 6mW, respectively. The microbots are fabricated in a 3x3 lattice, maintaining a distance of 30 μm between them. After two-photon exposure, the sample goes through post-exposure baking at 95°C for 8 min. The polymerized microstructures were developed using standard SU-8 developer solution (KAYAKU Advanced Materials) for 15 min and then dried with nitrogen. Then, the sample is plasma cleaned for 20 min to remove excess dextran. In addition, the plasma treatment increases the wettability of the SU-8 microbots.[42,43]

Optical Setup: Bright-field imaging is performed using a custom inverted optical microscope equipped with a 4X magnification objective (Nikon; NA = 0.13) and a high-sensitivity CMOS camera (Hamamatsu Orca-Flash 2.8). Patterns of green light (520 nm) are generated using a digital light processing (DLP) projector (Texas Instruments DLP Lightcrafter 4500) coupled to the same microscope objective used for imaging through a dichroic mirror.[31,33]

Bacterial Strain Costruction: For all the experiments, the *E. coli* strain AUYG, constructed from the strain AB1557 Δ*unc*: : *cmR* was used.[33] Using lambda red recombination with the recombination plasmid pKD46[44] we deleted the gene cheY responsible for the tumbling behavior of bacteria. We replaced it with the KnR cassette flanked by 50 bp homology amplified using template pKD4 (using the following primers: for: GCAAAAATTAGTGCCGGACAGGCGATACGTATTTAAAT CAGGAGTGTGAAGTGTAGGCTGGAGCTGCTTC, rev: CTGAATGCTCGTC

© 2023 The Authors. Advanced Functional Materials published by Wiley-VCH GmbH

AGCAGGTTTGATTGATGGTTGCATCATAGTCG-CATCCATGGGAATTAG CCATGGTCC). PCR reactions confirmed the desired genotype; we thus obtained a strain AB1557 Δ*unc*: : *cmR* Δ*cheY*: : *knR*. Then, it was transformed with the plasmid pBAD-His C encoding the SAR86 γ-proteobacterial photorhodopsin (PR) (a kind gift from Judith Armitage, University of Oxford) to obtain a smooth swimmer strain whose speed can be controlled with light. The obtained strain was similar to the strain AD57 used in [30].

Bacterial Growth Protocol: *E. coli* colonies from frozen stocks were grown overnight at 30°C on LB agar plates supplemented with ampicillin (100 μg ml^{-1}). A colony is picked and cultivated overnight at 30°C at 200 rpm in 10 ml of Terrific Broth (TB), a highly enriched bacterial growth media, with ampicillin. After 12–14 h, the overnight culture was diluted 100 times into 5 ml of Terrific Broth (TB) containing ampicillin and grown at 30°C, 200 rpm for 5 h. Then all-trans-retinal (20 μM) and L-arabinose (1 mM) were added to ensure expression and proper folding of PR in the membrane. The cells are collected after 1 h of induction by centrifugation at 1300 × g for 5 min at room temperature. The supernatant is removed. 100 μl of a motility solution consisting of double distilled water containing 0.02% Tween20 (Sigma–Aldrich) is added to the collected cells gently avoiding the resuspension of the pellet. After 20 min, 100 μl of the supernatant is collected into a different eppendorf tube and the centrifugation step is repeated. This allows for selecting only the highly motile bacteria for the experiment. This washing procedure was repeated two times in total; then, the cells were re-suspended at the desired concentration (OD). This motility solution allows the cells to remain motile without allowing growth or replication, so the concentration of the cells remained constant throughout the experiments.

Sample Preparation: The substrate with microbots was covered with a glass coverslip (previously plasma-treated) and hermetically sealed with UV glue (Norland Optical Adhesive NOA81) on opposing sides, see Figure S2c (Supporting Information). The distance between the coverslip and the glass substrate is maintained by placing a spacer 100 μm thick in the UV glue before sealing the cavity. 40 μL of the prepared bacterial suspension was injected into the glass cavity and was completely sealed on the remaining two sides by the application of Vacuum grease (Sigma–Aldrich). This step is necessary to cut off the system from surrounding oxygen and to avoid the generation of flows in the sample. The microbots detach from the substrate as soon as the bacterial suspension reaches the fabrication site and dissolves the underlying dextran sacrificial layer. The use of ionic species in the bacterial suspension is strictly regulated to avoid any surface charge interactions between the free-floating microbots and the glass surfaces. Bacteria deplete oxygen in around 2–5 min for OD = 2.0. Once this happens, the bacteria swim only where green light (520 nm) is projected, with their speed increasing as a function intensity of the projected light.[31]

Supporting Information

Supporting Information is available from the Wiley Online Library or from the author.

Acknowledgements

The research leading to these results has received funding from the European Research Council under the ERC Grant Agreement No. 834615 (R.D.L.). O.S.B. and R.D.L have received funding from Marie Sklodowska-Curie actions under Grant agreement no. 812780.

Open Access Funding provided by Universita degli Studi di Roma La Sapienza within the CRUI-CARE Agreement.

Conflict of Interest

The authors declare no conflict of interest.

Data Availability Statement

The data that support the findings of this study are available from the corresponding author upon reasonable request.

Keywords

active matters, biohybrid microrobots, microswimmers

Received: December 19, 2022
Revised: March 2, 2023
Published online:

[1] V. Lecault, A. K. White, A. Singhal, C. L. Hansen, *Curr. Opin. Chem. Biol.* **2012**, *16*, 381.
[2] H. Yin, D. Marshall, *Curr. Opin. Biotechnol.* **2012**, *23*, 110.
[3] S. Maruo, J. T. Fourkas, *Laser Photonics Rev.* **2008**, *2*, 100.
[4] R. W. Carlsen, M. Sitti, *Small* **2014**, *10*, 3831.
[5] L. Ricotti, B. Trimmer, A. W. Feinberg, R. Raman, K. K. Parker, R. Bashir, M. Sitti, S. Martel, P. Dario, A. Menciassi, *Sci. Rob.* **2017**, *2*, 1.
[6] V. A. Webster-Wood, M. Guix, N. W. Xu, B. Behkam, H. Sato, D. Sarkar, S. Sanchez, M. Shimizu, K. K. Parker, *Bioinspir. Biomim.* **2023**, *18*, 015001.
[7] D. B. Weibel, P. Garstecki, D. Ryan, W. R. DiLuzio, M. Mayer, J. E. Seto, G. M. Whitesides, *Proc. Natl. Acad. Sci. USA* **2005**, *102*, 11963.
[8] B. Behkam, M. Sitti, *Appl. Phys. Lett.* **2007**, *90*, 2.
[9] A. Sahari, D. Headen, B. Behkam, *Biomed. Microdevices* **2012**, *14*, 999.
[10] J. Bastos-Arrieta, A. Revilla-Guarinos, W. E. Uspal, J. Simmchen, *Front. Robot. AI* **2018**, *5*, 97.
[11] R. Di Leonardo, L. Angelani, D. Dell'Arciprete, G. Ruocco, V. Iebba, S. Schippa, M. P. Conte, F. Mecarini, F. De Angelis, E. Di Fabrizio, *Proc. Natl. Acad. Sci.* **2010**, *107*, 9541.
[12] L. Angelani, R. Di Leonardo, *New J. Phys.* **2010**, *12*, 113017.
[13] A. Kaiser, A. Peshkov, A. Sokolov, B. Ten Hagen, H. Löwen, I. S. Aranson, *Phys. Rev. Lett.* **2014**, *112*, 1.
[14] N. Koumakis, A. Lepore, C. Maggi, R. Di Leonardo, *Nat. Commun.* **2013**, *4*, 1.
[15] S. J. Park, H. Bae, J. Kim, B. Lim, J. Park, S. Park, *Lab Chip* **2010**, *10*, 1706.
[16] Z. Gao, H. Li, X. Chen, H. P. Zhang, *Lab Chip* **2015**, *15*, 4555.
[17] G. Vizsnyiczai, G. Frangipane, C. Maggi, F. Saglimbeni, S. Bianchi, R. Di Leonardo, *Nat. Commun.* **2017**, *8*, 1.
[18] D. Kim, A. Liu, E. Diller, M. Sitti, *Biomed. Microdevices* **2012**, *14*, 1009.
[19] O. Felfoul, M. Mohammadi, S. Taherkhani, D. De Lanauze, Y. Zhong Xu, D. Loghin, S. Essa, S. Jancik, D. Houle, M. Lafleur, L. Gaboury, M. Tabrizian, N. Kaou, M. Atkin, T. Vuong, G. Batist, N. Beauchemin, D. Radzioch, S. Martel, *Nat. Nanotechnol.* **2016**, *11*, 941.
[20] S. Martel, C. C. Tremblay, S. Ngakeng, G. Langlois, *Appl. Phys. Lett.* **2006**, *89*, 233904.
[21] B. W. Park, J. Zhuang, O. Yasa, M. Sitti, *ACS Nano* **2017**, *11*, 8910.
[22] J. Jiang, Z. Yang, A. Ferreira, L. Zhang, *Adv. Intell. Syst.* **2022**, *4*, 2100279.
[23] C. Maggi, F. Saglimbeni, M. Dipalo, F. De Angelis, R. Di Leonardo, *Nat. Commun.* **2015**, *6*, 1.
[24] V. Linder, B. D. Gates, D. Ryan, B. A. Parviz, G. M. Whitesides, *Small* **2005**, *1*, 730.
[25] J. M. Walter, D. Greenfield, C. Bustamante, J. Liphardt, *Proc. Natl. Acad. Sci.* **2007**, *104*, 2408.

© 2023 The Authors. Advanced Functional Materials published by Wiley-VCH GmbH

16163028, 0, Downloaded from https://onlinelibrary.wiley.com/doi/10.1002/adfm.202214801 by University Di Roma La Sapienza, Wiley Online Library on [11/09/2023]. See the Terms and Conditions (https://onlinelibrary.wiley.com/terms-and-conditions) on Wiley Online Library for rules of use; OA articles are governed by the applicable Creative Commons License

[26] S. Bianchi, F. Saglimbeni, R. Di Leonardo, *Phys. Rev. X* **2017**, *7*, 011010.
[27] O. Sipos, K. Nagy, R. Di Leonardo, P. Galajda, *Phys. Rev. Lett.* **2015**, *114*, 258104.
[28] A. P. Berke, L. Turner, H. C. Berg, E. Lauga, *Phys. Rev. Lett.* **2008**, *101*, 038102.
[29] E. Lauga, W. R. DiLuzio, G. M. Whitesides, H. A. Stone, *Biophys. J.* **2006**, *90*, 400.
[30] J. Arlt, V. A. Martinez, A. Dawson, T. Pilizota, W. C. Poon, *Nat. Commun.* **2018**, *9*, 1.
[31] G. Frangipane, D. Dell'Arciprete, S. Petracchini, C. Maggi, F. Saglimbeni, S. Bianchi, G. Vizsnyiczai, M. L. Bernardini, R. Di Leonardo, *Elife* **2018**, *7*, e36608.
[32] S. Goh, R. G. Winkler, G. Gompper, *New J. Phys.* **2022**, *24*, 093039.
[33] H. Massana-Cid, C. Maggi, G. Frangipane, R. Di Leonardo, *Nat. Commun.* **2022**, *13*, 1.
[34] F. A. Lavergne, H. Wendehenne, T. Bäuerle, C. Bechinger, *Science* **2019**, *364*, 70.
[35] J. Happel, H. Brenner, *Low Reynolds number hydrodynamics: With special applications to particulate media*, Vol. *1*, Springer, Berlin, **1983**.
[36] A. Búzás, L. Kelemen, A. Mathesz, L. Oroszi, G. Vizsnyiczai, T. Vicsek, P. Ormos, *Appl. Phys. Lett.* **2012**, *101*, 041111.
[37] S. Bianchi, G. Vizsnyiczai, S. Ferretti, C. Maggi, R. Di Leonardo, *Nat. Commun.* **2018**, *9*, 4476.
[38] E. Steager, C.-B. Kim, J. Patel, S. Bith, C. Naik, L. Reber, M. J. Kim, *Appl. Phys. Lett.* **2007**, *90*, 263901.
[39] E. B. Steager, M. S. Sakar, D. H. Kim, V. Kumar, G. J. Pappas, M. J. Kim, *J. Micromech. Microeng.* **2011**, *21*, 035001.
[40] W. Hu, K. S. Ishii, Q. Fan, A. T. Ohta, *Lab Chip* **2012**, *12*, 3821.
[41] M. J. Villangca, D. Palima, A. R. Banas, J. Glückstad, *Light: Sci. Appl.* **2016**, *5*, e16148.
[42] J. Izdebska-Podsiadły, in *Non-Thermal plasma technology for polymeric materials*, Elsevier, Amsterdam **2019**, pp. 159–191.
[43] F. Walther, P. Davydovskaya, S. Zürcher, M. Kaiser, H. Herberg, A. M. Gigler, R. W. Stark, *J. Micromech. Microeng.* **2007**, *17*, 524.
[44] K. A. Datsenko, B. L. Wanner, *Proc. Natl. Acad. Sci.* **2000**, *97*, 6640.

© 2023 The Authors. Advanced Functional Materials published by Wiley-VCH GmbH

16163028, 0, Downloaded from https://onlinelibrary.wiley.com/doi/10.1002/adfm.202214801 by University Di Roma La Sapienza, Wiley Online Library on [11/09/2023]. See the Terms and Conditions (https://onlinelibrary.wiley.com/terms-and-conditions) on Wiley Online Library for rules of use; OA articles are governed by the applicable Creative Commons License